A Consistent AVHRR Visible Calibration Record Based on Multiple Methods Applicable for the NOAA Degrading Orbits. Part I: Methodology

RAJENDRA BHATT

Science Systems and Applications, Inc., Hampton, Virginia

DAVID R. DOELLING

NASA Langley Research Center, Hampton, Virginia

BENJAMIN R. SCARINO, ARUN GOPALAN, AND CONOR O. HANEY

Science Systems and Applications, Inc., Hampton, Virginia

PATRICK MINNIS AND KRISTOPHER M. BEDKA

NASA Langley Research Center, Hampton, Virginia

(Manuscript received 5 February 2016, in final form 13 July 2016)

ABSTRACT

The 35-yr NOAA Advanced Very High Resolution Radiometer (AVHRR) observation record offers an excellent opportunity to study decadal climate variability, provided that all participating AVHRR instruments are calibrated on a consistent radiometric scale. Because of the lack of onboard calibration systems, the solar imaging channels of the AVHRR must be vicariously calibrated using invariant Earth targets as a calibrated reference source. The greatest challenge in calibrating the AVHRR dataset is the orbit degradation of the NOAA satellites, which eventually drift into a terminator orbit several years after launch. Therefore, the invariant targets must be characterized over the full range of solar zenith angles (SZAs) sampled by the satellite instrument.

This study outlines a multiple invariant Earth target calibration approach specifically designed to account for the degrading NOAA orbits. The desert, polar ice, and deep convective cloud (DCC) invariant targets are characterized over all observed SZAs using *NOAA-16* AVHRR measurements, which are referenced to the *Aqua* MODIS Collection 6 calibration via direct transfer of the MODIS calibration to the *NOAA-16* AVHRR instrument using simultaneous nadir overpass (SNO) observations over the North Pole. The multiple invariant target calibrations are combined using the inverse of their temporal variance to optimize the resulting calibration stability. The *NOAA-18* AVHRR gains derived using the desert, polar ice, and DCC targets, as well as from SNO, were found consistent within 1%, thereby validating that the *Aqua* MODIS calibration is effectively transferred to the reference calibration targets. The companion paper, Part II, applies the methodology across the AVHRR record to derive the sensor-specific calibration coefficients.

1. Introduction

Quantitative interpretation of satellite imager data for scientific applications is highly dependent on accurate and consistent calibrations of the imager's various spectral channels. Knowledge of this dependency is especially important for the development of climate data records (CDRs), which are often used to monitor various aspects of climate change. Longer records of climate parameters are necessary for detecting meaningful trends, which can only be established by the use of a series of satellite imagers that have similar characteristics. The Advanced Very High Resolution Radiometer (AVHRR) is one type of imager that has been operating in one of three versions over a significant time span, having flown on the TIROS, NOAA, and MetOp series of sun-synchronous satellites since 1978. The AVHRR is equipped with an

Corresponding author address: Rajendra Bhatt, Science Systems and Applications, Inc., 1 Enterprise Pkwy., Suite 200, Hampton, VA 23666.
E-mail: rajendra.bhatt@nasa.gov

DOI: 10.1175/JTECH-D-16-0044.1

onboard calibration system for its infrared channels, but it lacks similar capabilities for its visible and near-infrared channels. Therefore, to enhance its utility for climate studies, it is necessary to develop the most accurate calibrations possible for each of the AVHRR solar channels and to achieve interinstrument consistency with uncertainty estimates that can be used to characterize trends in any derived climate parameter.

The AVHRR instruments were launched in both afternoon and morning sun-synchronous polar orbits, providing a continuous overlapping set of morning (AM) and afternoon (PM) pair observations over most of the record. The AVHRR Global Area Coverage (GAC) format is available with a nominal pixel resolution of 4 km and the sensor has four to six spectral channels, depending on the build phase. The dependence on AVHRR for environmental retrievals has been diminished since the advent of well-calibrated sun-synchronous imagers, such as the Moderate Resolution Imaging Spectroradiometer (MODIS) on *Terra* and *Aqua*, and the Visible Infrared Imaging Radiometer Suite (VIIRS) on the *Suomi National Polar-Orbiting Partnership* (*SNPP*) satellite. Nominally, retrievals using MODIS data should be superior to those based on AVHRR data because MODIS employs onboard solar diffusers to monitor and correct for the degradation of the visible bands. MODIS data are available with a nominal pixel resolution of 1 km, and the sensor has 36 spectral bands. Additionally, the *Terra* and *Aqua* sun-synchronous orbits are maintained at their nominal equatorial crossing times, ensuring that there is no local time drift in the long-term record. In contrast, the AVHRR instrument lacks an onboard calibration system to track the fluctuations in the solar channel signals. The greatest challenge in quantifying the AVHRR on-orbit calibration fluctuations is the degrading sun-synchronous orbits of the NOAA satellites, which eventually drift into a terminator orbit over several years. Invariant Earth targets used for calibration must also be characterized over the range of solar and viewing angles encountered during the local time drift of the NOAA satellites.

The vicarious calibration of the AVHRR visible sensors is an ongoing 30-yr effort. In fact, many of the modern postlaunch calibration techniques currently in use were initiated and improved for the purpose of calibrating AVHRR. Calibration methods were developed to utilize Rayleigh scattering and glint over clear-sky ocean, as well as stable desert, polar ice, global clear-sky domain, and tropical bright high-cloud Earth targets (Brest and Rossow 1992; Kaufman and Holben 1993; Kogan et al. 1996; Loeb 1997; Masonis and Warren 2001; Staylor 1990; Vermote and Kaufman 1995; Wu and Zhong 1994; Nagaraja Rao and Chen 1995). Radiative transfer models (RTMs) have been used to predict TOA radiances over actively monitored ground sites to calibrate AVHRR instruments (Frouin and Gautier 1987; Teillet et al. 1990). Simultaneous overpass ray-matched (SOR) aircraft and AVHRR visible pairs were designed to transfer the aircraft instrument calibration to the AHVRR sensor (Abel et al. 1993; Holben et al. 1990; Smith et al. 1988; Whitlock et al. 1990). Later, the AVHRR sensors were more routinely calibrated over desert (Nagaraja Rao and Chen 1995, 1999) and polar ice (Tahnk and Coakley 2001, 2002) targets to provide time-dependent calibration coefficients.

Following the launch of the well-calibrated MODIS sensors, AVHRR and MODIS could be intercalibrated using simultaneous nadir overpass (SNO) radiance pairs (Heidinger et al. 2002). Furthermore, AVHRR and Tropical Rainfall Measuring Mission (TRMM) Visible and Infrared Scanner (VIRS), as well as AVHRR AM and PM satellites, were intercalibrated using near-simultaneous ray-matched radiance pairs (Doelling et al. 2001). The Hu et al. (2004) deep convective cloud (DCC) calibration approach was successfully applied to monitor the radiometric stability of AVHRR sensors (Doelling et al. 2004). Desert and polar ice pseudoinvariant calibration sites (PICS) were characterized using MODIS observations and were applied across many AVHRR sensors (Heidinger et al. 2010; Uprety and Cao 2011; Wu et al. 2010; Wu et al. 2013a). Concurrently, AVHRR and MODIS SNO intercalibrations were performed over multiple platforms (Wu et al. 2006; Heidinger et al. 2010). Remarkably, very few studies have attempted to compare, reconcile, and combine the various AVHRR visible gains from the numerous calibration methods (Che and Price 1992; Molling et al. 2010; Heidinger et al. 2010).

This study employs a uniform sensor calibration approach for the AVHRR channel 1 (Ch1) and Ch2 records, combining the calibration results of multiple invariant Earth target techniques. Arabia-1, Libya-1, Libya-4, and Niger-1 desert PICS; Dome-C and Greenland polar ice PICS; and tropical DCC are used to evaluate the AVHRR sensor stability and to transfer the *Aqua* MODIS reference calibration over the AVHRR satellite record. The multiple PICS approach reduces the impact of the natural reflectance variability of an individual target. This is accomplished by weighting the contribution of the individual PICS calibration by the inverse of their temporal variability to produce the combined optimized calibration result. Instead of characterizing the PICS utilizing MODIS observations, which do not encompass the entire solar zenith angle (SZA) range of NOAA satellites drifting into a terminator orbit, the PICS are characterized using *NOAA-16* (*N16*) AVHRR observations. Hereafter,

TABLE 1. Summary of spectral coverage of AVHRR VIS, NIR, SWIR, and IR channels.

Channel No.	AVHRR/1		AVHRR/2	AVHRR/3
	TIROS-N (μm)	*N6*, *N8*, *N10* (μm)	*N7*, *N9*, *N11*, *N12*, *N14* (μm)	*N15*–*N19*, *MetOp-A* and *MetOp-B* (μm)
1	0.55–0.90	0.58–0.68	0.58–0.68	0.58–0.68
2	0.725–1.10	0.725–1.10	0.725–1.10	0.725–1.00
3A	—	—	—	1.58–1.64
3B	3.55–3.93	3.55–3.93	3.55–3.93	3.55–3.93
4	10.50–11.50	10.50–11.50	10.30–11.30	10.30–11.30
5	—	—	11.50–12.50	11.50–12.50

for simplicity, the individual NOAA satellites are indicated with the abbreviation *Nx*, where *x* refers to the satellite number. The *N16* AVHRR visible radiances are first referenced to, or intercalibrated with, *Aqua* MODIS using the SNO approach, which also accounts for any temporal degradation in the responsivity of the AVHRR sensor. Also, the *N16* AVHRR visible band spectral response functions (SRFs) are more similar across the AVHRR instrument record than each compared to MODIS; thus, the required spectral band corrections are minimal. The final overall calibration, which we are calling multiple invariant targets referenced to *Aqua* MODIS (MITRAM), is validated against all of the possible NOAA and *Aqua* MODIS satellite pair SNO calibrations during the MODIS era. The consistency of the multiple independent calibration gains provides the overall uncertainty of the MITRAM calibration.

The study is organized into two papers. This paper describes the methodology, whereas the companion paper describes the implementation of the calibration methodology across the entire AVHRR record and provides the associated calibration coefficients, uncertainty, and validation results. Here, section 2 describes the AVHRR instruments and GAC processing. Section 3 highlights the AVHRR SRFs and the derivation of the spectral band adjustment factors (SBAFs), designed to account for spectral band differences. The SNO, PICS, and DCC calibration approaches, as well as the combining of multiple calibration gains, are discussed in section 4. The *N18* AVHRR calibration results based on the SNO and multiple invariant target approaches are discussed in section 5. Last, section 6 contains the conclusions of this study.

2. AVHRR instruments and GAC processing

The first AVHRR sensor was flown on the Television and Infrared Observation Satellite (TIROS-N), which was launched in October 1978. Since then, there have been several versions of the AVHRR carried on its successors, which include the *N6*–*N19*, *MetOp-A*, and *MetOp-B* satellites. The AVHRR instruments were built in three phases, which are referred to as AVHRR/1, AVHRR/2, and AVHRR/3, respectively. The AVHRR/1 instrument was a four-channel radiometer with spectral coverage ranging from 0.55 to 11.30 μm (Ch1: 0.55–0.90 μm, Ch2: 0.725–1.10 μm, Ch3: 3.55–3.93 μm, and Ch4: 10.50–11.50 μm). The AVHRR/2 instrument included all four channels of AVHRR/1 and an extra thermal infrared channel (Ch5: 11.50–12.50 m). The spectral channels of the AVHRR/3 instrument are slightly different from those of AVHRR/2, and include an additional channel in the shortwave infrared (SWIR) region (Ch3A: 1.58–1.64 m) to enhance daytime snow–ice discrimination and aerosol retrievals (Ignatov et al. 2004). The spectral details of the AVHRR/1–AVHRR/3 channels are presented in Table 1.

The host NOAA satellites carrying the AVHRR instruments did not include any system to maintain their sun-synchronous orbit. As a result, the satellites drift from their nominal orbit over time. The drift rate increases quadratically and leads to a continuously changing equator crossing time, as shown in Fig. 1 (NOAA 2015). TIROS-N, *N7*, *N9*, *N11*, *N14*, *N16*, *N18*, and *N19* are launched in afternoon orbits, and their ascending node continuously progresses toward later in the afternoon. Beginning with *N11*, the afternoon orbiters were launched into a 1330 equatorial crossing time (ECT) track rather than a 1430 ECT track. Note that the satellite orbits beginning with *N16* were designed to delay the onset of the degradation by modifying the initial inclination angle (Price 1991). On the other hand, the descending node of the morning orbiters, including *N6*, *N8*, *N10*, *N12*, *N15*, and *N17*, shift toward earlier in the morning. The *MetOp-A* and *MetOp-B* satellites are maintained in morning orbits and have a descending node time of ~0930 ECT.

a. GAC data

The AVHRR level 1B GAC format data with a nominal pixel resolution of 1.1 km × 4.4 km were obtained from the NOAA Comprehensive Large Array-Data Stewardship System (CLASS) (http://www.class.ngdc.noaa.gov/saa/products/welcome). The binary-format GAC data were unpacked, extracted, and interpreted according to the

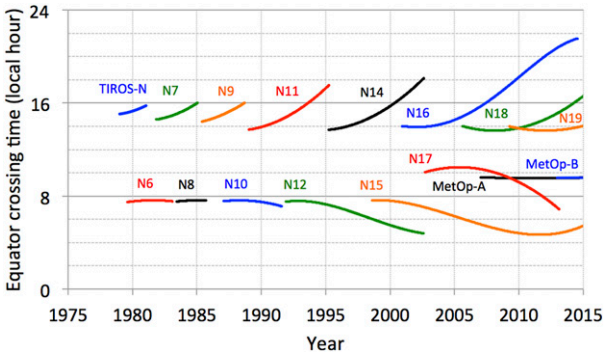

FIG. 1. Equator crossing times for the NOAA PM (ascending node) and AM (descending node) orbiter satellites continuously change over time due to orbital drift.

NOAA Polar Orbit Data (POD) and KLM user's guide. The radiometric quantization is 10 bits for all AVHRR sensors.

b. AVHRR/3 dual- to single-gain conversion

For the AVHRR/1 and AVHRR/2 sensors, the digital counts are proportional to radiance and a single gain is valid over the entire count range. However, the AVHRR/3 sensors use a "split gain" or "dual gain" setting for channels 1, 2, and 3A in order to enhance their radiometric sensitivity at low radiance levels (albedo $< \sim 25\%$). The nominal gain was set at 50% for counts less than the "break count" or "switch count," and at 150% for greater counts (Heidinger et al. 2010).

To facilitate uniform processing across the AVHRR record, the dual-gain counts C_{dual} are first converted to equivalent single-gain counts C_{single} to be linearly proportional to radiance. Following the methods of Heidinger et al. (2010), and using the nominal calibration coefficients provided by the NOAA POD and KLM user's guides, C_{dual} is converted to C_{single}. For dual-gain counts below the break point of intersection Split,

$$C_{\text{single}} = C_{\text{off}} + 0.5(C_{\text{dual}} - C_{\text{off}}), \tag{1}$$

where the low-gain offset C_{off} is defined by the NOAA platform-specific nominal count gain $\text{Slope}_{\text{nom}}$ and offset $\text{Intercept}_{\text{nom}}$ coefficients as

$$C_{\text{off}} = -(\text{Intercept}_{\text{nom}}/\text{Slope}_{\text{nom}}). \tag{2}$$

For dual-gain counts above the Split,

$$C_{\text{single}} = C_{\text{high}} + 1.5(C_{\text{dual}} - \text{Split}), \tag{3}$$

where the high-gain offset C_{high} is defined as follows:

$$C_{\text{high}} = C_{\text{off}} + 0.5(\text{Split} - \text{Intercept}_{\text{nom}}). \tag{4}$$

The $\text{Slope}_{\text{nom}}$, $\text{Intercept}_{\text{nom}}$, and Split values for each channel are listed in Tables D.1–D.6 (*N15*), D.2-7 (preflight AVHRR, *N16*), D.3-4 (*N17*), D.4-4 (*N18*), D.5-4 (*MetOp-A*), and D.6-4 (*N19*) within the KLM User's Guide and online (http://www.ncdc.noaa.gov/oa/pod-guide/ncdc/docs/klm/html/d/app-d.htm), where they are denoted as the low albedo range Slope, Intercept, and points of intersection, respectively. For Ch1 and Ch2, the GAC high- and low-gain ratios were set to 3, whereas for Ch3a they were set to 7. The dual-to-single-gain count conversion equations described above will still be true for Ch3a by replacing the 0.5 in Eq. (1) and Eq. (4) with 0.25, and the 1.5 in Eq. (3) with 1.75.

c. AVHRR space count

It has been reported that the AVHRR space count (C_0), or the space-view zero count, does not match the prelaunch values of either the ITT Corp. manuals or the NOAA POD or KLM user's guides, and instead varies on orbit (Ignatov et al. 2005). The desert, polar ice, and DCC Earth invariant target calibration methods do not directly measure the C_0 and must rely on an a priori C_0. Although the AVHRR instrument was designed with a space clamp to dampen out any space-view count oscillations, C_0 can vary by up to 0.5 counts over the satellite record (Mitchell 2001). To simplify the calibration application, it is preferable to have a single C_0 value valid over the entire satellite record.

A simple test was performed to determine C_0 and its stability over time. Because it was found that C_0 is within 0.1 count of the night count over the unlit portion of the earth (Ignatov et al. 2005), C_0 was computed by averaging all pixels with a SZA greater than 110° over one orbit. A near-equinox orbit was selected at the beginning and end of the satellite record. The near-equinox orbit was chosen so that C_0 can be observed under the same spacecraft solar conditions. Although a more thorough C_0 analysis is warranted following Ignatov et al. (2005), it is beyond the scope of this study.

Excepting *N8*, *N9*, and *N10*, the range of the pixel-level C_0 over an orbit is within three counts. For *N8* Ch2, the C_0 distribution over an orbit was noisier at the end of the record (Fig. 2b) than at the beginning (Fig. 2a). Similar results were found for *N8* Ch1 and for *N9* Ch1 and Ch2 (not shown). Figure 2c shows that the beginning-orbit *N10* C_0 distribution is broad, centered at 35 counts with low residual count noise. The end-orbit C_0 is shifted by one count from the beginning-orbit C_0 (Fig. 2d). The beginning and end-of-record C_0 difference is less than 0.5 counts for all satellite instruments and channels, except for *N6*, *N10*, *N15*, and *N16* Ch1, for which the C_0 difference is within one count. Also, for *N10* Ch2, the C_0 difference is 1.5.

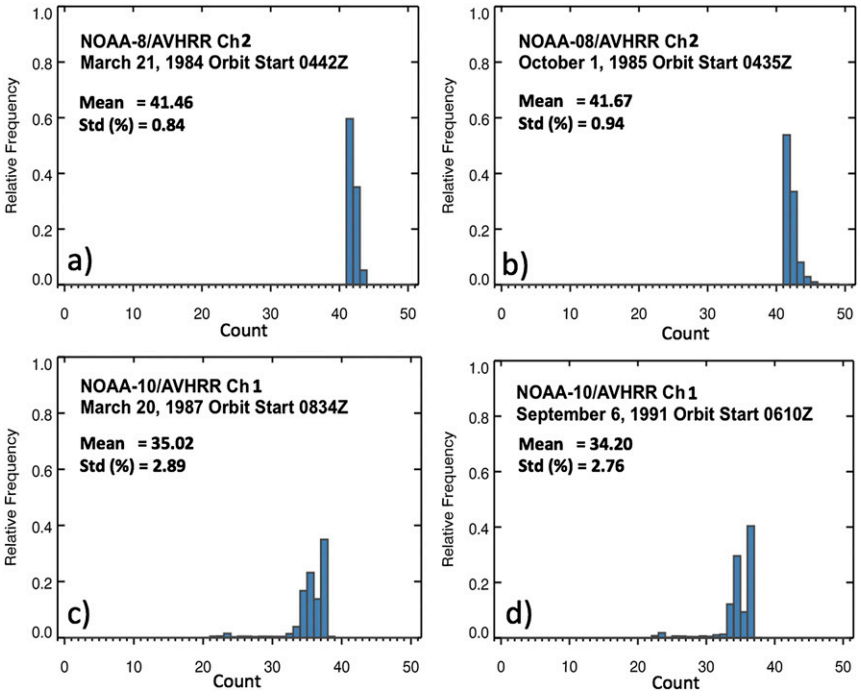

FIG. 2. (a) The frequency distribution of the *N8* AVHRR Ch2 (0.86 μm) channel nighttime space counts over one orbit on 21 Mar 1984. (b) As in (a), but for 1 Oct 1985. (c) The frequency distribution of the *N10* AVHRR Ch1 (0.65 μm) channel nighttime space counts over one orbit on 20 Mar 1987. (d) As in (c), but for 6 Sep 1991. The associated mean count and Std (%) are also shown. The count units are 10-bit single gain.

The channel-specific sensor record C_0 values were computed by averaging the beginning- and end-of-record C_0, and are listed in Doelling et al. (2016, hereafter Part II). The C_0 values are compared with the Clouds from the AVHRR Extended (CLAVR-x) dataset, which are obtained from Table 2 of Li et al. (2015), and were found to be within 1.5 counts—excepting *N10* Ch1 and Ch2, *N6* Ch1, and *N8* Ch2. Figures 2a and 2b clearly show that the *N8* Ch2 C_0 should be closer to 41.5 than 39.4.

3. Spectral band adjustments

a. AVHRR spectral response functions

The AVHRR SRFs were obtained from the NOAA Center for Satellite Applications and Research (STAR) program (http://www.star.nesdis.noaa.gov/smcd/spb/fwu/homepage/AVHRR/spec_resp_func/index.html). They are an improvement over the SRFs contained in the NOAA POD and KLM user's guides because all known errors have been corrected on versions on the STAR website. The AVHRR and MODIS sensor SRFs are highlighted in Fig. 3. A simulated atmospheric transmittance spectrum for a vertical path computed from MODTRAN using the maritime aerosol model, 23-km visibility, and the *U.S. Standard Atmosphere, 1976* (COESA 1976) is also shown in the background with a dashed line. The AVHRR imagers belonging to the same development phase have similar spectral band characteristics, except for the much wider TIROS-N visible (VIS) band. Small differences also exist in the SRFs of the AVHRR/3 and AVHRR/2 sensors. The *Aqua* MODIS SRF is narrower than any of the corresponding AVHRR bands, and it does not include any water vapor absorption bands.

b. Spectral band adjustment factors

Ignoring these spectral differences can cause potential biases in the cross calibration of AVHRR to MODIS, as well as between pairs of AVHRR instruments. The spectral band adjustment relies on the knowledge of the spectral signature of each Earth target, which is unique and dependent on the incoming solar irradiance, target reflectivity, and atmospheric column absorption. A ratio of band-specific solar constants, computed by convolving the incoming solar irradiance spectra with the sensor SRFs, accounts for the solar irradiance imparity at TOA but is not adequate to capture the differences in the sensor response due to the latter two factors. This study employs an SBAF for each reference and target sensor pair following

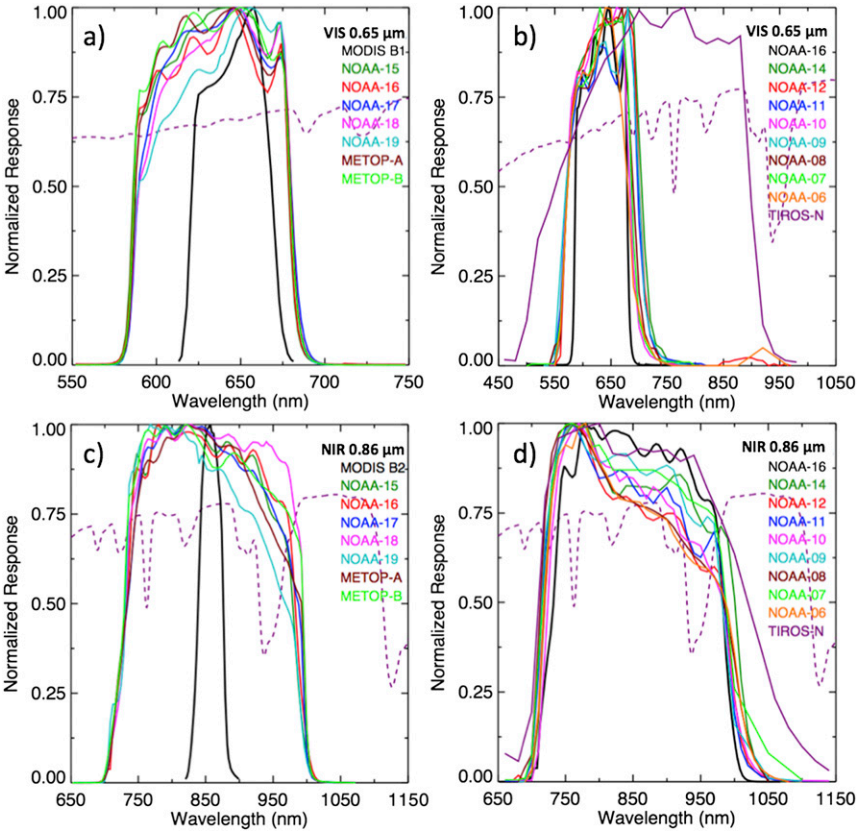

FIG. 3. SRF comparison between MODIS and AVHRR/3 sensors for AVHRR (a) Ch1 and (c) Ch2. SRF comparison between *N16* and AVHRR/1/2 sensors for AVHRR (b) Ch1 and (d) Ch2. Atmospheric transmittance spectra for a vertical path computed from MODTRAN using the maritime aerosol model, 23-km visibility, and the *U.S. Standard Atmosphere 1976* (COESA 1976) are also shown in the background with a dashed line.

the approach of Scarino et al. (2016), in which the target-specific footprint hyperspectral TOA radiances measured by the Scanning Imaging Absorption Spectrometer for Atmospheric Chartography (SCIAMACHY) instrument are first convolved with the SRFs of the target and reference sensors in order to estimate pseudoimager radiance pairs for these sensors. The SBAF is then the slope of regression of the pseudoradiance pairs. The SBAF is applied to the reference sensor radiances to arrive at spectrally corrected radiances for the target sensor. Although the SCIAMACHY measurements are not temporally coincident with either the AVHRR or MODIS measurements, they are assumed to capture the same typical surface, atmospheric, and cloud conditions over intercalibration and PICS domains. The concept of a priori SCIAMACHY-based SBAFs was validated by determining the consistency of the calibration gains derived over various calibration targets (Morstad et al. 2011; Doelling et al. 2012; Bhatt et al. 2014a; Scarino et al. 2012, 2016).

To derive the *N16* Ch1 and *Aqua* MODIS band 1 SNO SBAF, a linear regression through the origin (force fit) of the *N16* Ch1 and MODIS band 1 pseudoradiance pairs was computed from 18 886 SCIAMACHY footprints acquired over the North Pole domain during 2002–10 (Fig. 4a). The computed SBAF for this sensor pair is 1.025, which indicates that the observed MODIS band 1 radiances must be adjusted by 2.5% to achieve spectral consistency with *N16* Ch1. For this case, the band-specific solar constant ratio is 1.027 based on the Thuillier et al. (2003) solar spectra and is very close to the SCIAMACHY-based SBAF. The corresponding Ch2 SBAF equals 0.924 for the same sensor pairs over the SNO domain and is shown in Fig. 4b. However, the solar constant ratio, which accounts for only the incoming solar spectra, is 1.039 and is 12% greater than from the SCIAMACHY SBAF. This suggests that the snow reflectance spectra, as well as near-IR (NIR) water vapor absorption over the SNO domain, differ significantly between MODIS band 2 and *N16* Ch2. The standard error of the force fit pseudoradiance pair regression is 0.75% and 3.8% for Ch1 and Ch2, respectively. The greater standard error of Ch2 indicates

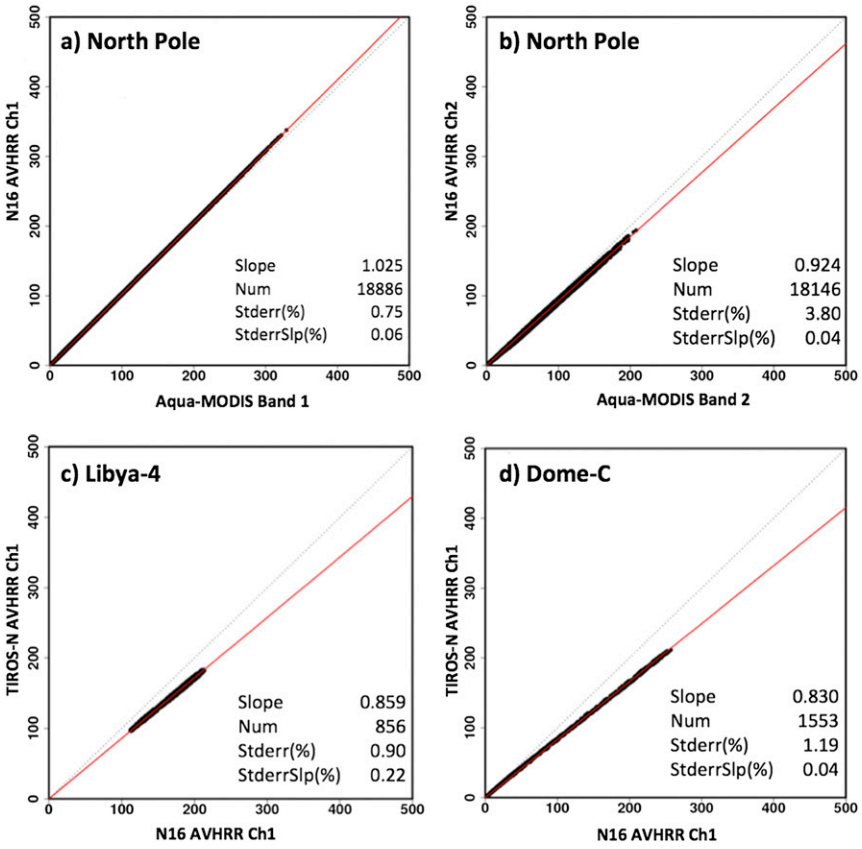

FIG. 4. The SBAF regressions of SCIAMACHY-based pseudoradiances ($W\,m^{-2}\,\mu m^{-1}\,sr^{-1}$) for *N16* AVHRR and *Aqua* MODIS over the North Pole SNO domain: (a) Ch1 (0.65 μm) and (b) Ch2. The SBAF regressions of TIROS-N and *N16* AVHRR Ch1 over (c) Libya-4 and (d) Dome-C. The linear regression through the origin (red line) and line of unity (black dotted line), as well as the regressions statistics, are also shown. The standard error of the predicted value (StdErr) and standard error of the slope (StderrSlp) of the regression are given (%).

greater variability in the NIR spectra than in the visible spectra, mainly due to the NIR water vapor absorption.

The force fit of the TIROS-N and *N16* Ch1 pseudoradiance pairs for Libya-4 and Dome-C are 0.859 (Fig. 4c) and 0.830 (Fig. 4d), respectively. The desert and polar ice SBAF difference is 3.5%, which clearly demonstrates the need for site-specific SBAFs. The band-specific solar constant ratio is 0.857, which is similar to the Libya-4 SCIAMACHY SBAF. Therefore, the TIROS-N Ch1 SBAF based on SCIAMACHY accounts for both the mismatched incoming solar spectra in part and the difference in the Earth-reflected spectra caused by the NIR water vapor absorption bands.

4. Calibration methods

AVHRR calibration coefficients are derived using up to three different calibration approaches, which are summarized in the following sections.

a. SNO calibration approach

The SNO approach uses the *Aqua* MODIS sensor as the reference and transfers its calibration to AVHRR by matching coincident, collocated, and coangled radiance/count pairs from the two instruments. The technique relies on the assumption that the reference and target satellites will, on average, measure the same radiance (or count equivalent), within a small time window and narrow angular matching tolerance. This method is applicable only to AVHRR sensors operating during the *Aqua* MODIS record (2002–present) and has been employed in the past by numerous researchers (Heidinger et al. 2002; Doelling et al. 2004; Heidinger et al. 2010). In this study, SNO locations—where the AVHRR and MODIS orbits intersect within 15 min of each other—are identified using orbital prediction software based on North American Air Defense Command (NORAD) two-line elements (TLEs). For each

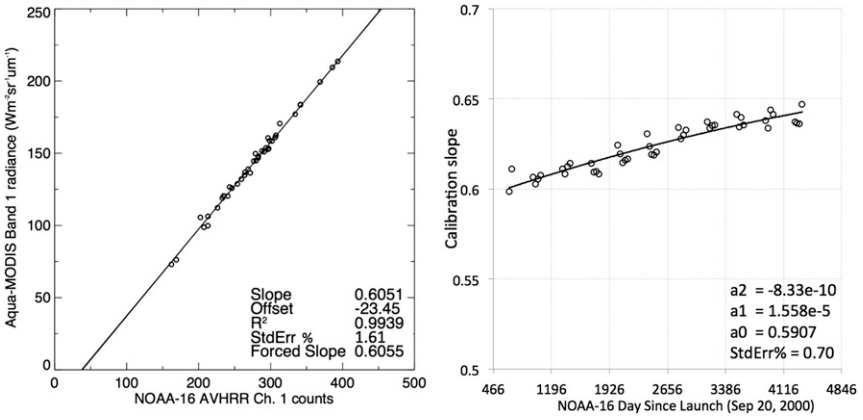

FIG. 5. (a) The observed monthly *N16* AVHRR Ch1 count and *Aqua* MODIS band 1 radiance SNO pairs during July 2003. The linear regression slope, offset, and R^2 statistics are given in the lower right. The solid black line represents the linear regression through the C_0 of 38.9 (forced slope) with the StdErr in %. (b) The monthly force slopes and second-order temporal regression line for *N16* AVHRR Ch1 during 2002–13. The associated coefficients and statistics are given in the lower right. The count units are 10-bit single gain.

SNO, the AVHRR and MODIS pixel data are averaged into a 50-km-diameter field of view (FOV) to mitigate the pixel navigational error, as well as any advective displacement of clouds due to the 15-min difference between the two measurements (Wielicki et al. 2008). The averaged 50-km FOV AVHRR counts (C) and MODIS radiance ($\mathrm{Rad_{MODIS}}$) pairs are linearly regressed through the AVHRR space count C_0 to compute the gain (g) on a monthly basis according to Eq. (5),

$$(\mathrm{Rad_{MODIS}})(\mathrm{SBAF_{AVHRR/MODIS}})(\mu_{0\mathrm{AVHRR}}/\mu_{0\mathrm{MODIS}}) = g(C - C_0), \quad (5)$$

where SBAF is the MODIS-to-AVHRR spectral band adjustment factor and μ_0 is the cosine of the SZA.

Figure 5a shows the linear regression through the C_0 of 38.9 (force fit) for the *N16* AVHRR Ch1 count and *Aqua* MODIS band 1 radiance SNO pairs during July 2003. The force fit and linear regression slopes are within 0.1% for this case, thereby indicating that the predetermined C_0 agrees with the linear regression space count. The force fit standard error (StdErr) is 1.61%, which can be attributed to the changing atmospheric conditions within 15 min and the variability of the FOV spectra about the mean spectra as represented by the SCIAMACHY-based SBAF. A second-order polynomial fit is applied to describe the temporal trend of the monthly *N16* Ch1 gains computed from the SNO approach (Fig. 5b). Figure 5b reveals that the radiometric responsivity of the sensor has diminished by ~7% during its 12-yr operation time.

b. *Pseudoinvariant calibration site approach*

PICS are bright and stable natural ground targets wherein the average reflectance during clear-sky settings, and for a given set of viewing and solar angular conditions, remains nearly stable over time. An ideal PICS would have 1) high surface reflectance to maximize the signal-to-noise ratio (SNR), 2) high spatial homogeneity to reduce the errors due to misregistration, 3) high elevation to mitigate the effects of water vapor and aerosols, 4) low total column water vapor with minimal presence of clouds and vegetation, 5) a near-Lambertian surface to minimize the bidirectional reflectance distribution function (BRDF) effects, and 6) long-term radiometric stability (Cosnefroy et al. 1996; Helder et al. 2010). The most promising PICS suitable for postlaunch calibration and validation of satellite instruments have been found over the North African and Saudi Arabian deserts (Cosnefroy et al. 1996). The ice caps of Greenland and Antarctica are other temporally stable targets that have been successfully used for calibrating AVHRR (Loeb 1997; Masonis and Warren 2001; Tahnk and Coakley 2001, 2002), the Advanced Along-Track Scanning Radiometer-2 (AATSR-2) (Smith and Cox 2013), and the MODIS (Wu et al. 2013b; Doelling et al. 2015) sensors in past studies.

The 20 candidate desert sites listed by Cosnefroy et al. (1996) were evaluated for temporal stability, clear-sky probability, and spatial homogeneity using 13 years of *Aqua* MODIS Collection 6 (C6) level 1b band 1 data. The MODIS C6 visible calibration was found to be stable within 1% over a decade (Doelling et al. 2015). Clear-sky conditions are determined by a spatial

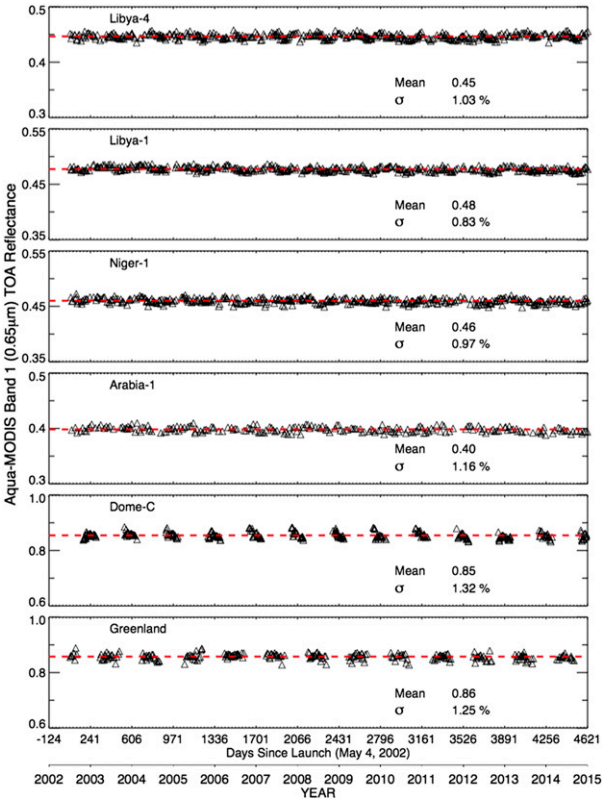

FIG. 6. The *Aqua* MODIS band 1 (0.65 μm) TOA clear-sky anisotropic-corrected reflectance time series over (from top to bottom) Libya-4, Libya-1, Niger-1, Arabia-1, Dome-C, and Greenland using near-nadir observations from 2002–14 reveal the excellent temporal stability of these PICS.

homogeneity test as described by Bhatt et al. (2014b). The *Aqua* MODIS TOA near-nadir clear-sky reflectances were anisotropically corrected using a semi-empirical approach based on a linear combination of two kernel functions as described by Roujean et al. (1992). The evaluation revealed that the four most suitable desert sites are Libya-1 (24.42°N, 13.35°E), Libya-4 (28.55°N, 23.40°E), Arabia-1 (18.88°N, 46.76°E), and Niger-1 (19.67°N, 9.81°E longitude). Two polar ice cap regions, Dome-C (75.1°S, 123.4°E) and Greenland (75.5°N, 39.5°W), were also selected for a total six PICS. The size of the region of interest is 0.5°× 0.5° for all six PICS. Figure 6 shows the *Aqua* MODIS band 1 (0.65 μm) TOA clear-sky anisotropic-corrected reflectance time series derived for the six selected sites. Based on the *Aqua* MODIS observations, the six PICS are found to be stable within 1.5% for over a decade.

To use the desert and polar ice PICS for transferring calibrations from *Aqua* MODIS to AVHRR, a PICS-specific directional model (DM) is developed to characterize its TOA radiance as a function of μ_0. Owing to the slowly degrading orbits of the NOAA satellites, the DM TOA radiances must be characterized over the entire range of observed SZA. Because the *Aqua* orbit is well maintained, the MODIS observations over the PICS have a limited SZA range. For example, the subtropical deserts are observed only by *Aqua* or *Terra* MODIS with SZA $< 60°$. Bhatt et al. (2015) also illustrated with a simple extrapolation of the radiance with μ_0 that the MODIS-based DMs are inadequate for characterizing desert targets for large SZAs and are therefore not suitable for AVHRR calibration purposes. Because the *N16* satellite drifted into a terminator orbit during its operation, the lifetime observations from its onboard AVHRR instrument provides a unique opportunity to construct the PICS DMs that sufficiently cover the required SZA range. This study first transfers the *Aqua* MODIS band 1 and 2 calibrations to *N16* AVHRR Ch1 and Ch2, respectively, using the SNO approach. The PICS DMs are then derived using the site-specific TOA radiances measured by the *N16* AVHRR under clear-sky conditions during 2001–14. For 2001, the *N16* AVHRR gains are computed by simply extrapolating the second-order temporal regression of the SNO gains. The *N16* AVHRR Ch1 pixel-level spatial homogeneity thresholds used to identify clear-sky conditions over Libya-1, Libya-4, Arabia-1, Niger-1, Dome-C, and Greenland are 5, 8, 6, 12, 10, and 20 counts, respectively. Only near-nadir observations having viewing zenith angles (VZA) within 10° for the deserts and 5° for the polar ice PICS are utilized in order to mitigate anisotropic effects. Applying the DMs to calibrate another AVHRR operating during the MODIS era, and then comparing the DM calibration with its SNO-based calibration can validate the effectiveness of these empirically derived DMs.

Bhatt et al. (2014b) found that under near-nadir viewing conditions, the *Aqua* MODIS visible radiances over Libya-4 are slightly brighter for backward-scattering conditions [relative azimuth angles (RAA) $< 90°$] than in the forward-scattering (RAA $> 90°$) direction, especially for overhead-sun conditions. A similar observation was also reported by Govaerts (2015), who studied the effects of sand dune orientation on the surface bidirectional reflectance factor of Libya-4 using a 3D radiative transfer model and the Libya-4 topography computed from the 30-m-resolution Advanced Spaceborne Thermal Emission and Reflection Radiometer (ASTER) digital elevation model. We observed a similar effect over all four desert PICS using *N16* AVHRR measurements. Figure 7a displays the Libya-4 DM derived from the *N16* Ch1 (0.65 μm) calibrated radiances normalized to an Earth–sun distance of 1 AU. The second-order regression coefficients define the DM, and the associated standard

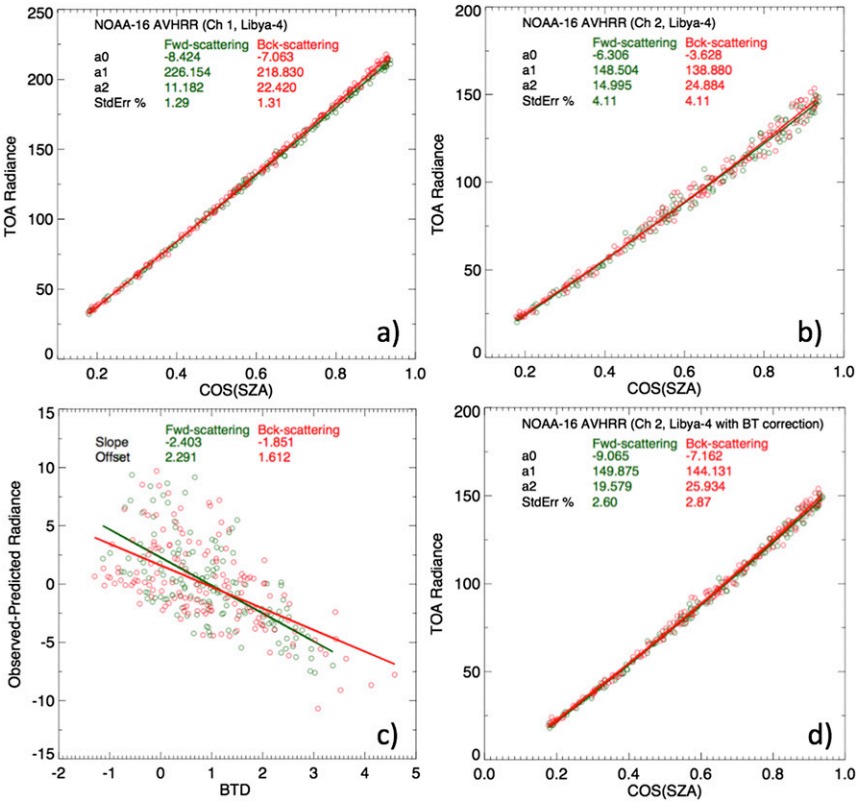

FIG. 7. Libya-4 DMs derived from near-nadir *N16* AVHRR radiances ($W\,m^{-2}\,\mu m^{-1}\,sr^{-1}$) for (a) Ch1 and (b) Ch2. The second-order regression coefficients and StdErr (%) are also given. (c) A BTD correction model of 11 minus 12 μm is derived to normalize the AVHRR Ch2 radiances to zero BTD in order to account for the effect of WV variability on the DM. (d) The revised Ch2 model after applying the BTD correction shows an uncertainty reduction of ~35%.

error of the fit represents the natural variability of the site over the *N16* record. The corresponding Libya-4 *N16* Ch2 DM is shown in Fig. 7b. The large standard error is a result of the TOA radiance variability owed to the NIR water absorption. To account for the columnar atmospheric water vapor absorption on the Ch2 DM radiance, the 11- and 12-μm brightness temperature difference (BTD) is correlated with the observed-minus-predicted (DM in Fig. 7b) radiance (see Fig. 7c). Previous studies have correlated the BTD with the precipitable water vapor content (Yu and Wu 2010). Because all of the AVHRR 11-μm SRFs (12-μm SRFs also) are comparable, and because the IR channels are calibrated with an onboard blackbody, the BTDs are assumed to be consistent for all of the sensors and are therefore used to approximate the impact of the water vapor (WV) over the record. The linear fits are used to normalize all Ch2 radiances to zero BTD, and the DM is revised using the normalized radiances. The revised *N16* Ch2 DM is illustrated in Fig. 5d, which shows a 35% reduction in the standard error. Because AVHRR/1 instruments did not carry a 12-μm channel, the Ch2 DM was applied without any BTD correction to those sensors. It was also found that Niger-1 is not suitable, and therefore it is not used for calibrating NOAA morning-orbit AVHRRs. Even though the surface reflectance is large, the variation of water vapor over Niger-1 is large owing to its proximity to the tropics, where long pathlengths are common.

In contrast with the desert PICS, the TOA radiances for polar ice targets have no clear dependency upon the scattering direction. Also, BTD corrections to account for water vapor variability are not required for the Ch2 DMs due to the dry atmosphere of high-altitude polar ice regions (Uprety and Cao 2011). Therefore, only a single DM is derived for both Greenland and Dome-C targets. The Dome-C DMs for Ch1 and Ch2 are shown in Fig. 8. The polar ice targets exhibit a larger DM standard error compared to desert sites, which is likely due to the lower SNR at the larger observed SZA. The DM coefficients and associated standard errors for all six PICS are listed in Table 2. Finally, the predicted TOA radiances from the PICS DMs (DM_{PICS}) are used to

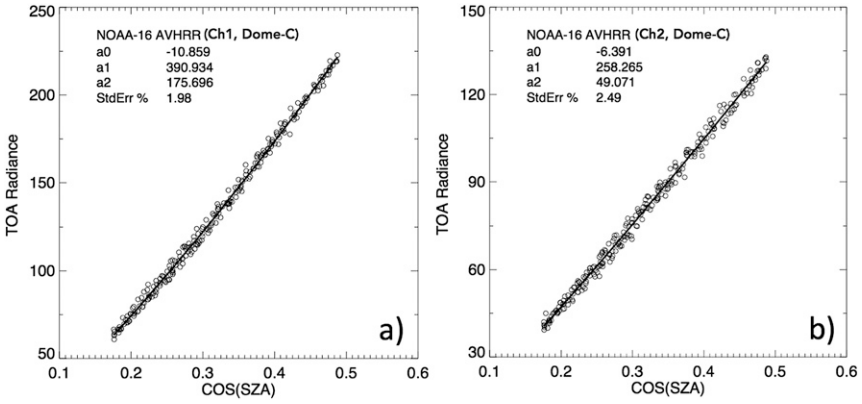

FIG. 8. Dome-C DMs derived from *N16* AVHRR radiances ($W\,m^{-2}\,\mu m^{-1}\,sr^{-1}$) for (a) Ch1 and (b) Ch2. The second-order regression coefficients and StdErr (%) are also given.

compute the gain from the AVHRR sensor count (C) and space count (C_0) for a given μ_0, RAA, or scattering direction, and BTD, where applicable, using Eq. (6),

$$\mathrm{DM}_{\mathrm{PICS}}(\mu_0, \mathrm{RAA}, \mathrm{BTD})\mathrm{SBAF}_{\mathrm{AVHRR}/N16} = g(C - C_0), \quad (6)$$

where SBAF is the *N16*-to-AVHRR spectral band adjustment factor.

c. *DCC calibration approach*

DCC are the coldest and the brightest of all terrestrial invariant targets. They are located near the tropopause, where the impact of water vapor and aerosols on satellite measurements are minimal. With the highest SNR and nearly flat reflected solar spectra for wavelengths less than 1 μm, DCCs provide a more stable reflectance than the invariant deserts and polar ice sites. Many studies have used DCC for calibrating a wide range of satellite sensors, including AVHRR (Doelling et al. 2004), geostationary Earth-orbiting satellite imagers (Morstad et al. 2011; Doelling et al. 2011), *Aqua* and *Terra* MODIS (Wu et al. 2013b; Doelling et al. 2015), and *SNPP* VIIRS (Bhatt et al. 2014a; Wang and Cao 2015). The DCC method relies on the assumption that the DCC cores produce a predictable statistical distribution of reflectances for a given set of angular conditions.

The baseline method is described by Doelling et al. (2013). The AVHRR DCC pixels are identified over the tropical domain (±30° in latitude) by an 11-μm brightness temperature threshold of 205 K. To ensure a uniform cloud top and to reject optically thin clouds, a spatial homogeneity test is performed on both visible radiance and IR BT measurements. A DCC pixel passes the uniformity test if the given pixel and the surrounding

TABLE 2. PICS DM coefficients and associated standard errors.

Ch1 DM parameters (forward/backscattering)				
PICS	a0	a1	a2	StdErr (%)
Libya-4	−8.424/−7.063	226.153/218.83	11.182/22.42	1.1/1.3
Libya-1	−15.451/−13.675	268.626/258.975	−12.786/-0.135	1.3/1.3
Arabia-1	−9.241/−8.646	213.144/209.862	−3.504/3.326	1.6/1.6
Niger-1	−2.354/−1.685	212.557/208.980	28.661/36.191	2.9/2.7
Dome-C	−10.859	390.934	175.696	2.0
Greenland	−25.585	420.203	141.331	2.1
Ch2 DM parameters (forward/backscattering)				
PICS	a0	a1	a2	StdErr (%)
Libya-4	−9.065/−7.162	149.875/144.131	19.579/25.934	2.6/2.9
Libya-1	−13.429/−10.591	179.852/162.761	7.503/25.95	2.6/2.3
Arabia-1	−7.067/−6.125	145.1/137.569	3.634/13.578	4.0/3.9
Niger-1	−4.723/−5.99	147.206/151.435	25.722/23.432	4.5/5.8
Dome-C	−6.391	258.265	49.071	2.5
Greenland	−9.445	249.466	49.501	4.0

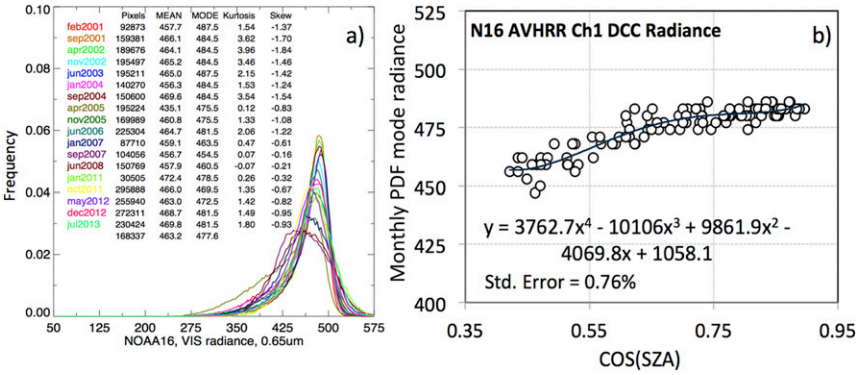

FIG. 9. (a) Monthly PDFs of *N16* AVHRR Ch1 (0.65 μm) DCC radiances (W m^{-2} μm^{-1} sr^{-1}). The number of pixels and DCC mean/mode radiance values are given for the months listed. (b) *N16* AVHRR Ch1 DCC monthly PDF mode radiance as a function of the cosine of the monthly mean SZA. The corresponding fourth-order regression coefficients and StdErr are also given.

eight-pixel standard deviation (Std) are less than 3% in the visible and 1 K in the IR. DCCs are nearly Lambertian and require minimal anisotropic corrections. The filtered AVHRR DCC pixels are normalized to nadir-viewing and overhead-sun conditions using the angular distribution model (ADM) developed by Hu et al. (2004). The baseline method restricts the SZA and VZA to be less than 40° to take advantage of the most isotropic part of the DCC reflectivity. The normalized DCC radiances are then compiled as monthly probability distribution functions (PDFs). The modes of the monthly histograms are tracked over time to monitor the stability of the sensor. It is assumed that a perfectly calibrated sensor will have consistent monthly mode, anisotropic-corrected DCC radiances.

For this study, the SZA constraint is increased to 75° in order to allow DCC calibration to be utilized over a longer time record of AVHRR data, during which the satellite orbit is degrading. To determine whether the monthly mode DCC radiances are consistent, the *N16* AVHRR is first calibrated using *Aqua* MODIS SNOs. Figure 9 (left panel) shows the monthly PDFs of the calibrated DCC radiances from *N16* Ch1. During the first few years after launch, the monthly PDF shape remains consistent. However, the monthly PDF shapes during near-terminator conditions (2007–08) are not similar. This is probably due to the inadequacy of the DCC ADM model. The monthly PDF DCC mode radiances are plotted as a function of the monthly mean $\boldsymbol{\mu_0}$ in Fig. 9 (right panel). A fourth-order polynomial fit is used to predict DCC mode radiance as a function of μ_0. The fit is the reference DM for the DCC calibration approach in this study. The DCC DM indicates that the monthly DCC PDF mode radiances are relatively flat for $\mu_0 > 0.7$ or for SZA $< 45°$, which means that the Hu et al. (2004) ADM anisotropic corrections are robust for SZA $< 45°$.

To calibrate the AVHRR sensors, the same baseline DCC calibration, with an extended SZA range of 75° utilizing the DCC DM, is followed. The predicted monthly DCC PDF mode radiance is obtained from the DCC DM [$\mathrm{DM_{DCC}}(\mu_0)$] and is spectrally adjusted (see section 3b) for the given AVHRR sensor ($\mathrm{SBAF_{AVHRR/\mathit{N16}}}$) to compute g from the monthly DCC mode count (C_{MODE}) with the C_0 removed using Eq. (7),

$$\mathrm{DM_{DCC}}(\mu_0)\mathrm{SBAF_{AVHRR/\mathit{N16}}} = \mathrm{gain}C_{\mathrm{MODE}}. \qquad (7)$$

To calibrate AVHRR Ch2 radiances using the DCC calibration, the same Ch1 $\mathrm{DM_{DCC}}(\mu_0)$ is used but the SBAF converts the same Ch1 radiance to the given AVHRR Ch2 radiance. This method is followed because MODIS band 2 saturates for large radiances, such as from DCC, and is therefore unable to provide a DCC mode radiance for Ch2. Because DCC are spectrally flat within 1 μm and are not impacted by water vapor absorption in the NIR, the AVHRR Ch1-to-Ch2 SBAF correction uncertainty should be small. This approach was validated using the DCC measurements from the *SNPP* VIIRS I1 (0.65 μm) and M7 (0.86 μm) bands. The observed DCC mode radiance for the M7 band, and the same predicted from the I1 band using the I1-to-M7 DCC SBAF factor, agrees within 0.3%.

d. Temporal trending and combining of gains

The computed AVHRR invariant target monthly gains are tracked over time to derive temporal trends that are characterized by a quadratic fit. Second-order temporal fits were also used to approximate the AVHRR sensor degradation in the Heidinger et al. (2010) and Li et al.

(2015) studies. The monthly gains (g) are regressed as a function of day since launch (dsl) using Eq. (8),

$$g = m_0 + m_1 \mathrm{dsl} + m_2 \mathrm{dsl}^2, \quad (8)$$

where the coefficients m_0, m_1, and m_2 are given in units of $\mathrm{W\,m^{-2}\,sr^{-1}\,\mu m^{-1}}$ per count, $\mathrm{W\,m^{-2}\,sr^{-1}\,\mu m^{-1}}$ per count per day, and $\mathrm{W\,m^{-2}\,sr^{-1}\,\mu m^{-1}}$ per count per days squared, respectively.

In this study, the resulting PICS calibration gains are further combined using an inverse-variance weighted regression approach in order to derive optimal mission-long calibration coefficients for the AVHRR sensors. The combined desert monthly gain (g_{comb}) time series is computed from weighting factors (w_i) based on the inverse of the variance ($1/\sigma_i^2$) using the individual PICS monthly gains (g_i) and Eq. (9),

$$g_{\mathrm{comb}} = \Sigma g_i w_i, \quad \text{where} \quad w_i = (1/\sigma_i^2)/\Sigma 1/\sigma_i^2. \quad (9)$$

A second-order least squares regression [Eq. (8)] is then performed through the combined desert monthly gains to derive the desert-based AVHRR gain trend. The same process is repeated with the Dome-C and Greenland monthly gains to derive the combined polar ice monthly gains from which the polar ice trend is computed. Finally, a similar inverse-variance weighting approach is followed to combine the DCC, desert, and polar ice monthly gains and derive the optimal MITRAM trend. For consistency throughout the AVHRR record, the SNO-based AVHRR gains (MODIS era only) are not used in computing the MITRAM AVHRR gains. However, during the MODIS time frame, the SNO results serve as a reference for evaluating the MITRAM gains.

5. Results and discussion

In this section, *N18* is used to demonstrate the MITRAM calibration approach. Figure 10 demonstrates good agreement between the individual PICS measurement gains. The agreement is greater during the beginning of the record than at the end due to the increasing SZA over time as the *N18* orbit degrades. The standard errors are based on the individual site trends (not shown).

The combined desert monthly gains derived from the four PICS, using the inverse-variance weighted approach and the corresponding second-order regression, are shown in Fig. 10. The combined desert standard error is 0.81%, which is less than any of the individual desert sites, which range between 0.95% and 1.52%. Combining the PICS calibration gains using an inverse-variance weighting approach reduces the impact of the least stable desert

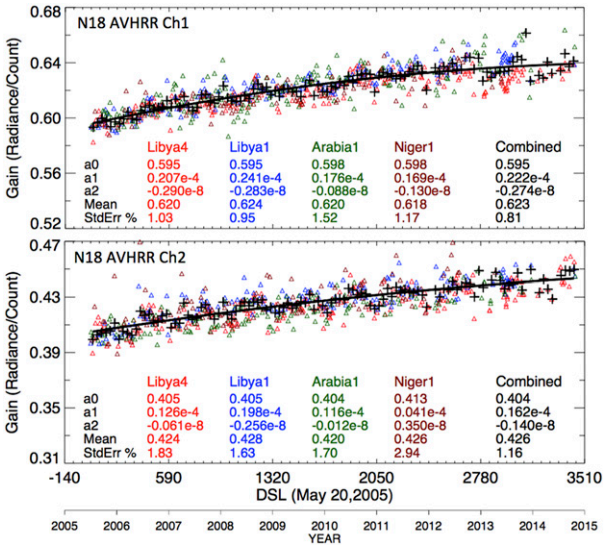

FIG. 10. *N18* AVHRR (top) Ch1 (0.65 μm) and (bottom) Ch2 (0.86 μm) gains derived using the Libya-4, Libya-1, Arabia-1, and Niger-1 PICS DMs. The combined monthly desert gains are plotted in black "+" and the associated quadratic regression is shown as the solid black line. The individual PICS and combined desert second-order regression coefficients, mean time line gains, and StdErr (%) are also given. The count and radiance units are 10-bit single gain and $\mathrm{W\,m^{-2}\,\mu m^{-1}\,sr^{-1}}$, respectively.

sites and increases the contributions from the more stable desert sites. The desert site stability may change over time; thus, this method does not rely on the most stable desert site over the whole record, but rather the most stable site only over the sensor record. Similar to Ch1, the Ch2 combined desert standard error is also less than those from the individual desert sites, which have a similar standard error of ~1.7%, except for Niger-1. The inverse-variance weighting approach has effectively reduced the contribution of Niger-1 to derive the combined desert calibration coefficients.

Figure 11 shows plots of *N18* AVHRR Ch1 and Ch2 gains derived using the Dome-C and Greenland PICS measurements. Because the observations over these two polar ice sites occur in opposite seasons, the measurements do not overlap and therefore the inverse-variance weighted approach is not beneficial here. Thus, the Dome-C and Greenland monthly mean gains are simply combined. Target temporal variability and inadequate referencing to the *Aqua* MODIS calibration impact the standard error of the gain. As expected the combined polar ice standard error is greater than the individual site standard error. The polar ice Ch1 standard errors are larger than for those deserts, as are the standard errors of the corresponding PICS DM. This is likely due to poor SNR over the poles, where the solar illumination is low and the sample size is lacking. There also seems to

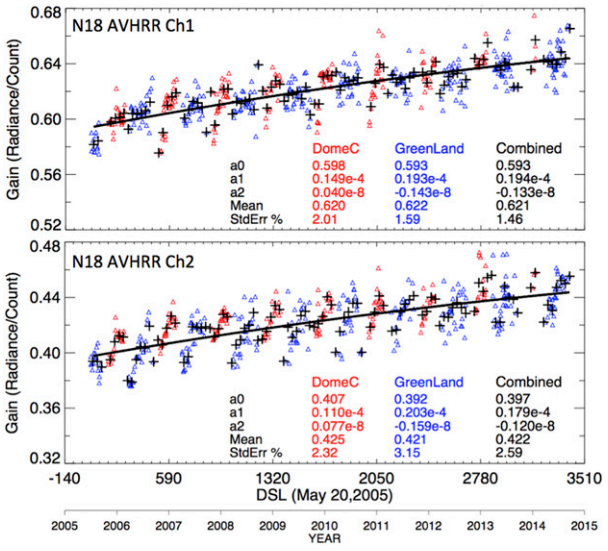

FIG. 11. As in Fig. 10, but using the Dome-C and Greenland PICS.

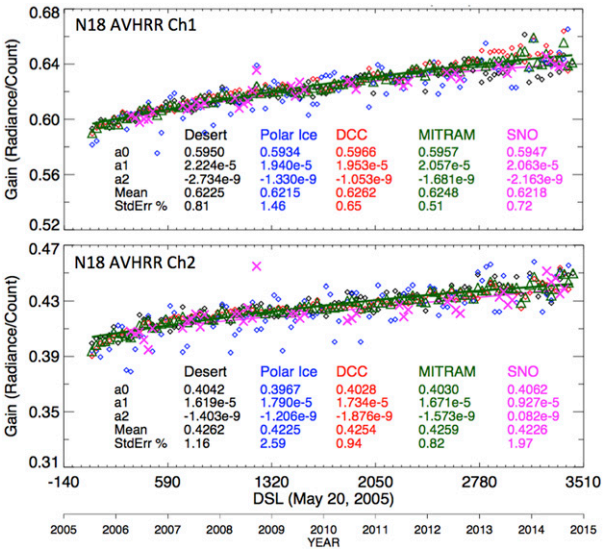

FIG. 12. *N18* AVHRR (top) Ch1 (0.65 μm) and (bottom) Ch2 (0.86 μm) MITRAM monthly gains plotted as green "Δ" derived from desert-, polar ice–, and DCC-based monthly gains using an inverse-variance weighting approach. The associated MITRAM quadratic regression is shown as the solid green line. The *Aqua* MODIS SNO monthly gains (magenta "X") and quadratic regression (solid magenta line) are also plotted for consistency analysis. The desert, polar ice, and DCC invariant targets, MITRAM, and SNO second-order regression coefficients; mean time line gains; and StdErr (%) are also given.

be a seasonal cycle in the Ch2 gains, which could be attributed to an increase in the snow grain size as the summer sun melts the snow. This cycle is not accounted for in the polar ice DM. An increase in the snow grain size reduces the surface reflectivity, especially for Ch2 (Nolin and Dozier 2000). However, the *N18* mean gain differences between Dome-C and Greenland are within 0.3% and 0.7% for Ch1 and Ch2, respectively. In fact the corresponding standard deviations of all six desert and polar ice PICS mean gains are 0.43% and 0.65%, respectively, which suggests that all six PICS DMs have successfully transferred the *Aqua* MODIS reference calibration.

The monthly desert-, polar ice–, DCC-, MITRAM-, and SNO-based gain trends for *N18* AVHRR are shown in Fig. 12. The MITRAM monthly gain trends are computed from the inverse-variance weighted average of the monthly desert, polar ice, and DCC gains. The second-order temporal regression statistics for the five time series are also shown. The gains show good agreement in both magnitude and trend. The differences among the mission-long mean gains computed from the desert, polar ice, DCC, and SNO approaches are minimal, within 1%, which implies two things: First, the PICS and DCC DMs based on *N16* AVHRR are accurately referenced to *Aqua* MODIS C6 calibration. Second, the SCIAMACHY-based SBAFs have effectively accounted for the spectral differences between the analogous AVHRR and MODIS channels, considering that each PICS has its own unique Earth-reflected spectra. The disadvantage of the polar AVHRR and MODIS SNO visible intercalibration approach is that the results are only available for half of the year. On the other hand, the MITRAM approach has the advantage of providing continuous monthly gains with a comparable or smaller temporal standard error, and therefore it is more suitable for accurately quantifying the AVHRR sensor calibration drift over time. The excellent agreement between the multiple approaches suggests that the PICS and DCC DMs discussed in this study have great potential to uniformly calibrate the historical AVHRR VIS and NIR record referenced to the *Aqua* MODIS calibration. The details of the calibration results for the complete AVHRR sensor series, associated uncertainties, and their comparison with other published studies are discussed in Part II.

6. Conclusions

Nearly four decades of continuous daily global observations from AVHRR reflective solar channels are invaluable for climate change studies and environmental applications. For quantitative utilizations of the AVHRR data in such studies, it is critical that the AVHRR sensors are uniformly calibrated by way of postlaunch, vicarious means. In this paper, we have presented three vicarious approaches of tracing the AVHRR VIS and NIR record to an *Aqua* MODIS C6 reference calibration. The SNO cross calibration utilizes near-coincident (within 15 min)

nadir matches between MODIS and AVHRR over the North Pole, and is a relatively simple and robust method for determining calibration coefficients of the AVHRR sensor. However, its application is limited to the AVHRR sensors during the MODIS time frame. Therefore, we have formulated two more generalized approaches—one based on the use of six PICS and a second that employs the tropical DCC invariant Earth target—that are used to consistently calibrate the historical and present AVHRR sensor record. The methods utilize the *N16* AVHRR-based DMs that characterize TOA radiances observed over the PICS and the DCC target as a function of SZA. Owing to the fact that the *N16* satellite gradually drifted into a terminator orbit and therefore encompasses all possible SZA as viewed by any AVHRR sensor over any Earth target, the proposed DMs are robust and can effectively account for the degrading orbits of the NOAA satellites during the calibration time frame. Prior to the construction of the DMs, the *N16* AVHRR Ch1 and Ch2 are cross calibrated with analogous MODIS bands using the SNO approach, thereby referencing the DMs to the *Aqua* MODIS calibration. The calibration results obtained from the six PICS and the DCC DMs are combined using an inverse-variance weighted averaging method in order to compute optimal MITRAM AVHRR gains.

The use of hyperspectral reflected solar spectra obtained from the SCIAMACHY instrument has been a key element in our study to account for the spectral differences between the AVHRR and MODIS bands. The spectral band adjustment relies on the knowledge of the spectral signature of the Earth target, which is unique and dependent on the incoming solar irradiance, target reflectivity, and atmospheric column absorption. Our studies have shown that not accounting for NIR absorption can cause a 12% bias in the MODIS band 2 and *N16* Ch2 SNO calibration slopes compared with only taking into account the solar incoming irradiance spectra. A unique SBAF was found for each calibration site or domain. For example, the TIROS-N and *N16* Ch1 SBAFs for Libya-4 and Dome-C are 0.859 and 0.830, respectively, a difference of 3.5%.

The *N18* AVHRR desert, polar ice, DCC invariant target and SNO gains were found to be consistent within 1%, which validates the invariant target *N16*-based DM approach for transferring the *Aqua* MODIS calibration reference obtained from the MODIS and *N16* SNOs. A thorough assessment of the calibration coefficients derived for all AVHRR sensors is provided in Part II.

Acknowledgments. The AVHRR satellite data were obtained from NOAA CLASS. The authors thank Karl-Göran Karlsson for independently comparing the MITRAM and PATMOS-X calibration coefficients, and Aisheng Wu for providing the MODTRAN-derived atmospheric transmittance data. Thanks to A. Heidinger for the helpful discussions. This research was supported by the NOAA Climate Data Record Program under Interagency Agreement NOAA-IA1-17982. The AVHRR calibration coefficients from this study are contained in the NOAA CDR of visible and near-infrared reflectance from GOES and AVHRR, version 1.0 (AVHRR radiances, NASA; doi:10.789/V5NK3C0J), and were used to produce the NOAA CDR of cloud and clear-sky radiation properties, version 1.0 (AVHRR cloud properties, NASA; doi:10.789/V5HT2M8T). An algorithm theoretical basis document (ATBD) is also available (Doelling and Minnis 2016).

REFERENCES

Abel, P., B. Guenther, R. N. Galimore, and J. W. Cooper, 1993: Calibration results for the *NOAA-11* AVHRR channels 1 and 2 from congruent path aircraft observations. *J. Atmos. Oceanic Technol.*, **10**, 493–508, doi:10.1175/1520-0426(1993)010<0493:CRFACA>2.0.CO;2.

Bhatt, R., D. R. Doelling, D. Morstad, B. R. Scarino, and A. Gopalan, 2014a: Desert-based absolute calibration of successive geostationary visible sensors using a daily exoatmospheric radiance model. *IEEE Trans. Geosci. Remote Sens.*, **52**, 3670–3682, doi:10.1109/TGRS.2013.2274594.

——, ——, A. Wu, X. Xiaong, B. R. Scarino, C. O. Haney, and A. Gopalan, 2014b: Initial stability assessment of S-NPP VIIRS reflective solar band calibration using invariant desert and deep convective cloud targets. *Remote Sens.*, **6**, 2809–2826, doi:10.3390/rs6042809.

——, ——, B. R. Scarino, A. Gopalan, and C. Haney, 2015: Toward consistent radiometric calibration of the NOAA AVHRR visible and near-infrared data record. *Earth Observing Systems XX*, J. J. Butler, X. Xiong, and X. Gu, Eds., International Society for Optical Engineering (SPIE Proceedings, Vol. 9607), 960703, doi:10.1117/12.2186816.

Brest, C. L., and W. B. Rossow, 1992: Radiometric calibration and monitoring of NOAA AVHRR data for ISCCP. *Int. J. Remote Sens.*, **13**, 235–273, doi:10.1080/01431169208904037.

Che, N., and J. C. Price, 1992: Survey of radiometric calibration results and methods for visible and near infrared channels of NOAA-7, -9 and -11 AVHRRs. *Remote Sens. Environ.*, **41**, 19–27, doi:10.1016/0034-4257(92)90057-Q.

COESA, 1976: *U.S. Standard Atmosphere, 1976*. NOAA, 227 pp.

Cosnefroy, H., M. Leroy, and X. Briottet, 1996: Selection and characterization of Saharan and Arabian desert sites for the calibration of optical satellite sensors. *Remote Sens. Environ.*, **58**, 101–114, doi:10.1016/0034-4257(95)00211-1.

Doelling, D. R., and P. Minnis, 2016: Calibration of historical and future AVHRR and GOES visible and near-infrared sensors. Algorithm Theoretical Basis Doc. CDRP-ATBD-0823, 50 pp. [Available online at https://www.ncdc.noaa.gov/sites/default/files/cdr-documentation/%3Cem%3EEdit%20Climate%20Data%20Record%3C/em%3E%20AVHRR%20Radiances%20-%20NASA/CDRP-ATBD-0823%20AVHRR%20Radiances%20-%20NASA%20C-ATBD%20(01B-30a)%20(DSR-1048).pdf.]

——, V. Chakrapani, P. Minnis, and L. Nguyen, 2001: The calibration of NOAA-AVHRR visible radiances with VIRS.

Preprints, *11th Conf. on Satellite Meteorology and Oceanography*, Madison, WI, Amer. Meteor. Soc., P5.29. [Available online at https://ams.confex.com/ams/11satellite/techprogram/paper_24401.htm.]

——, L. Nguyen, and P. Minnis, 2004: On the use of deep convective clouds to calibrate AVHRR data. *Earth Observing Systems IX*, W. L. Barnes and J. J. Butler, Eds., International Society for Optical Engineering (SPIE Proceedings, Vol. 5542), 281–289, doi:10.1117/12.560047.

——, D. Morstad, R. Bhatt, and B. R. Scarino, 2011: Algorithm theoretical basis document (ATBD) for deep convective cloud (DCC) technique of calibrating GEO sensors with Aqua-MODIS for GSICS. *2011 GSICS User's Workshop*, Oslo, Norway, EUMETSAT, 11 pp. [Available online at http://gsics.atmos.umd.edu/pub/Development/AtbdCentral/GSICS_ATBD_DCC_NASA_2011_09.pdf.]

——, C. Lukashin, P. Minnis, B. R. Scarino, and D. Morstad, 2012: Spectral reflectance corrections for satellite intercalibrations using SCIAMACHY data. *IEEE Geosci. Remote Sens. Lett.*, **9**, 119–123, doi:10.1109/LGRS.2011.2161751.

——, D. Morstad, B. R. Scarino, R. Bhatt, and A. Gopalan, 2013: The characterization of deep convective clouds as an invariant calibration target and as a visible calibration technique. *IEEE Trans. Geosci. Remote Sens.*, **51**, 1147–1159, doi:10.1109/TGRS.2012.2225066.

——, A. Wu, X. Xiong, B. Scarino, R. Bhatt, C. Haney, D. Morstad, and A. Gopalan, 2015: The radiometric stability and scaling of collection 6 Terra- and Aqua-MODIS VIS, NIR, and SWIR spectral bands. *IEEE Trans. Geosci. Remote Sens.*, **53**, 4520–4535, doi:10.1109/TGRS.2015.2400928.

——, R. Bhatt, B. R. Scarino, A. Gopalan, C. O. Haney, P. Minnis, and K. M. Bedka, 2016: A consistent AVHRR visible calibration record based on multiple methods applicable for the NOAA degrading orbits. Part II: Validation. *J. Atmos. Oceanic Technol.*, **33**, 2517–2534, doi:10.1175/JTECH-D-16-0042.1.

Frouin, R., and C. Gautier, 1987: Calibration of NOAA-7 AVHRR, GOES-5 and GOES-6 VISSR/VAS solar channels. *Remote Sens. Environ.*, **22**, 73–101, doi:10.1016/0034-4257(87)90028-9.

Govaerts, Y., 2015: Sand dune ridge alignment effects on surface BRF over the Libya-4 CEOS calibration site. *Sensors*, **15**, 3453–3470, doi:10.3390/s150203453.

Heidinger, A. K., C. Cao, and J. T. Sullivan, 2002: Using Moderate Resolution Imaging Spectroradiometer (MODIS) to calibrate advanced very high resolution radiometer reflectance channels. *J. Geophys. Res.*, **107**, 4702, doi:10.1029/2001JD002035.

——, W. C. Straka III, C. C. Molling, and J. T. Sullivan, 2010: Deriving an inter-sensor consistent calibration for the AVHRR solar reflectance data record. *Int. J. Remote Sens.*, **31**, 6493–6517, doi:10.1080/01431161.2010.496472.

Helder, D. L., B. Basnet, and D. L. Morstad, 2010: Optimized identification of worldwide radiometric pseudo-invariant calibration sites. *Can. J. Remote Sens.*, **36**, 527–539, doi:10.5589/m10-085.

Holben, B. N., Y. J. Kaufman, and J. D. Kendall, 1990: NOAA AVHRR visible and near-IR inflight calibration. *Int. J. Remote Sens.*, **11**, 1511–1519, doi:10.1080/01431169008955109.

Hu, Y., B. A. Wielicki, P. Yang, P. W. Stackhouse Jr., B. Lin, and D. F. Young, 2004: Application of deep convective cloud albedo observation to satellite-based study of the terrestrial atmosphere: Monitoring the stability of spaceborne measurements and assessing absorption anomaly. *IEEE Trans. Geosci. Remote Sens.*, **42**, 2594–2599, doi:10.1109/TGRS.2004.834765.

Ignatov, A., J. Sapper, S. Cox, I. Laszlo, N. R. Nalli, and K. B. Kidwell, 2004: Operational Aerosol Observations (AEROBS) from AVHRR/3 on board NOAA-KLM satellites. *J. Atmos. Oceanic Technol.*, **21**, 3–26, doi:10.1175/1520-0426(2004)021<0003:OAOAFO>2.0.CO;2.

——, C. Cao, and J. Sullivan, 2005: The usefulness of in-flight measurements of space count to improve calibration of the AVHRR solar reflectance bands. *J. Atmos. Oceanic Technol.*, **22**, 180–200, doi:10.1175/JTECH-1691.1.

Kaufman, Y. J., and B. N. Holben, 1993: Calibration of the AVHRR visible and near-IR bands by atmospheric scattering, ocean glint and desert reflection. *Int. J. Remote Sens.*, **14**, 21–52, doi:10.1080/01431169308904320.

Kogan, F. N., J. T. Sullivan, and P. B. Ciren, 1996: Testing post-launch calibration for the AVHRR sensor on world desert targets during 1985–1993. *Adv. Space Res.*, **17**, 47–50, doi:10.1016/0273-1177(95)00444-J.

Li, C., Y. Xue, Q. Liu, K. Ouzzane, and J. Zhang, 2015: Using SeaWiFS measurements to evaluate radiometric stability of pseudo-invariant calibration sites at top of atmosphere. *IEEE Geosci. Remote Sens. Lett.*, **12**, 125–129, doi:10.1109/LGRS.2014.2329138.

Loeb, N. G., 1997: In-flight calibration of NOAA AVHRR visible and near-IR bands over Greenland and Antarctica. *Int. J. Remote Sens.*, **18**, 477–490, doi:10.1080/014311697218908.

Masonis, S. J., and S. G. Warren, 2001: Gain of the AVHRR visible channel as tracked using bidirectional reflectance of Antarctic and Greenland snow. *Int. J. Remote Sens.*, **22**, 1495–1520, doi:10.1080/01431160121039.

Mitchell, R. M., 2001: In-flight characteristics of the space count of NOAA AVHRR channels 1 and 2. CSIRO Atmospheric Research Tech. Paper 52, 24 pp. [Available online at http://www.cmar.csiro.au/e-print/open/mitchellr_2001a.pdf.]

Molling, C. C., A. K. Heidinger, W. C. Straka, and X. Wu, 2010: Calibrations for AVHRR channels 1 and 2: Review and path towards consensus. *Int. J. Remote Sens.*, **31**, 6519–6540, doi:10.1080/01431161.2010.496473.

Morstad, D. L., D. R. Doelling, R. Bhatt, and B. R. Scarino, 2011: The CERES calibration strategy of the geostationary visible channels for CERES cloud and flux products. Earth Observing Systems *XVI*, J. J. Butler, X. Xiong, and X. Gu, Eds., International Society for Optical Engineering (SPIE Proceedings, Vol. 8153), 815316, doi:10.1117/12.894650.

Nagaraja Rao, C. R., and J. Chen, 1995: Inter-satellite calibration linkages for the visible and near-infrared channels of the Advanced Very High Resolution Radiometer on the NOAA-7, -9, and -11 spacecraft. *Int. J. Remote Sens.*, **16**, 1931–1942, doi:10.1080/01431169508954530.

——, and ——, 1999: Revised post-launch calibration of the visible and near-infrared channels of the Advanced Very High Resolution Radiometer (AVHRR) on the NOAA-14 spacecraft. *Int. J. Remote Sens.*, **20**, 3485–3491, doi:10.1080/014311699211147.

NOAA, 2015: Equatorial crossing time (ECT) for NOAA polar satellites. NOAA Center for Satellite Applications and Research, accessed 26 January 2016. [Available online at http://www.star.nesdis.noaa.gov/smcd/emb/vci/VH/vh_avhrr_ect.php.]

Nolin, A. W., and J. Dozier, 2000: A hyperspectral method for remotely sensing the grain size of snow. *Remote Sens. Environ.*, **74**, 207–216, doi:10.1016/S0034-4257(00)00111-5.

Price, J. C., 1991: Timing of NOAA afternoon passes. *Int. J. Remote Sens.*, **12**, 193–198, doi:10.1080/01431169108929644.

Roujean, J. L., M. J. Leroy, and P. Y. Deschamps, 1992: A bidirectional reflectance model of the Earth's surface for the correction of remote sensing data. *J. Geophys. Res.*, **97**, 20 455–20 468, doi:10.1029/92JD01411.

Scarino, B. R., D. R. Doelling, D. L. Morstad, R. Bhatt, C. Lukashin, and P. Minnis, 2012: Using SCHIAMACHY to improve corrections for spectral and differences when transferring calibration between visible sensors. *Earth Observing Systems XVII*, J. J. Butler, X. Xiong, and X. Gu, Eds., International Society for Optical Engineering (SPIE Proceedings, Vol. 8510), 85100Q, doi:10.1117/12.929767.

——, ——, P. Minnis, A. Gopalan, T. Chee, R. Bhatt, C. Lukashin, and C. Haney, 2016: A web-based tool for calculating spectral band difference adjustment factors derived from SCIAMACHY hyperspectral data. *IEEE Trans. Geosci. Remote Sens.*, **54**, 2529–2542, doi:10.1109/TGRS.2015.2502904.

Smith, D. L., and C. V. Cox, 2013: (A)ATSR solar channel on-orbit radiometric calibration. *IEEE Trans. Geosci. Remote Sens.*, **51**, 1370–1382, doi:10.1109/TGRS.2012.2230333.

Smith, G. R., R. H. Levin, P. Abel, and H. Jacobowitz, 1988: Calibration of the solar channels of the NOAA-9 AVHRR using high altitude aircraft measurements. *J. Atmos. Oceanic Technol.*, **5**, 631–639, doi:10.1175/1520-0426(1988)005<0631:COTSCO>2.0.CO;2.

Staylor, W. F., 1990: Degradation rates of the AVHRR visible channel for the NOAA 6, 7 and 9 spacecraft. *J. Atmos. Oceanic Technol.*, **7**, 411–423, doi:10.1175/1520-0426(1990)007<0411:DROTAV>2.0.CO;2.

Tahnk, W. R., and J. A. Coakley Jr., 2001: Improved calibration coefficients for NOAA-14 AVHRR visible and near-infrared channels. *Int. J. Remote Sens.*, **22**, 1269–1283, doi:10.1080/01431160151144341.

——, and ——, 2002: Improved calibration coefficients for *NOAA-12* and *NOAA-15* AVHRR visible and near-IR channels. *J. Atmos. Oceanic Technol.*, **19**, 1826–1833, doi:10.1175/1520-0426(2002)019<1826:ICCFNA>2.0.CO;2.

Teillet, P. M., P. N. Slater, Y. Ding, R. P. Santer, R. D. Jackson, and M. S. Moran, 1990: Three methods for the absolute calibration of the NOAA AVHRR sensors in-flight. *Remote Sens. Environ.*, **31**, 105–120, doi:10.1016/0034-4257(90)90060-Y.

Thuillier, G., M. Hersé, D. Labs, T. Foujols, W. Peetermans, D. Gillotay, P. C. Simon, and H. Mandel, 2003: The solar spectral irradiance from 200 to 2400 nm as measured by the SOLSPEC spectrometer from the Atlas and Eureca missions. *Sol. Phys.*, **214**, 1–22, doi:10.1023/A:1024048429145.

Uprety, S., and C. Cao, 2011: Using the Dome C site to characterize AVHRR near-infrared channel for consistent radiometric calibration. *Earth Observing Systems XVI*, J. J. Butler, X. Xiong, and X. Gu, Eds., International Society for Optical Engineering (SPIE Proceedings, Vol. 8153), 81531Y, doi:10.1117/12.892481.

Vermote, E., and Y. J. Kaufman, 1995: Absolute calibration of AVHRR visible and near- infrared channels using ocean and cloud views. *Int. J. Remote Sens.*, **16**, 2317–2340, doi:10.1080/01431169508954561.

Wang, W., and C. Cao, 2015: DCC radiometric sensitivity to spatial resolution, cluster size, and LWIR calibration bias based on VIIRS observations. *J. Atmos. Oceanic Technol.*, **32**, 48–60, doi:10.1175/JTECH-D-14-00024.1.

Whitlock, C. H., and Coauthors, 1990: AVHRR and VISSR satellite instrument calibration results for both cirrus and marine stratocumulus IFO periods. FIRE science results 1988, D. S. McDougal and H. S. Wagner, Eds., NASA Conf. Publ. 3083, 141–145.

Wielicki, B. A., D. R. Doelling, D. F. Young, N. G. Loeb, D. P. Garber, and D. G. MacDonnell, 2008: Climate quality broadband and narrowband solar reflected radiance calibration between sensors in orbit. *2008 IEEE International Geoscience and Remote Sensing Symposium: Proceedings*, Vol. 1, IEEE, I-257–I-260, doi:10.1109/IGARSS.2008.4778842.

Wu, A., and Q. Zhong, 1994: A method for determining the sensor degradation rates of NOAA AVHRR channels 1 and 2. *J. Appl. Meteor.*, **33**, 118–122, doi:10.1175/1520-0450(1994)033<0118:AMFDTS>2.0.CO;2.

——, C. Cao, and X. Xiong, 2006: Using MODIS to track calibration stability of the AVHRR on NOAA 15-18. *Remote Sensing and Modeling of Ecosystems for Sustainability III*, W. Gao and S. L. Ustin, Eds., International Society for Optical Engineering (SPIE Proceedings, Vol. 6298), 629812, doi:10.1117/12.681199.

——, X. Xiong, and A. Angal, 2013a: Deriving a MODIS-based calibration for the AVHRR reflective solar channels of the NOAA KLM operational satellites. *IEEE Trans. Geosci. Remote Sens.*, **51**, 1405–1413, doi:10.1109/TGRS.2012.2220780.

——, ——, D. R. Doelling, D. L. Morstad, A. Angal, and R. Bhatt, 2013b: Characterization of Terra and Aqua MODIS VIS, NIR, and SWIR spectral band calibration stability. *IEEE Trans. Geosci. Remote Sens.*, **51**, 4330–4338, doi:10.1109/TGRS.2012.2226588.

Wu, X., J. T. Sullivan, and A. K. Heidinger, 2010: Operational calibration of the Advanced Very High Resolution Radiometer (AVHRR) visible and near-infrared channels. *Can. J. Remote Sens.*, **36**, 602–616, doi:10.5589/m10-080.

Yu, F., and X. Wu, 2010: Water vapor correction to improve the operational calibration for NOAA AVHRR/3 channel 2 (0.85 μm) over a desert target. *Can. J. Remote Sens.*, **36**, 514–526, doi:10.5589/m10-077.